2-23-2023

Simplified demonstration of a new perivascular pump mechanism for glymphatic flow of interstitial fluid in the brain

Charles F. Babbs

Technical note:

Simplified demonstration of a new perivascular pump mechanism for glymphatic flow of interstitial fluid in the brain

Charles F. Babbs, MD, PhD, Weldon School of Biomedical Engineering,
Purdue University, February 23, 2023

Abstract

In a previous paper the author presented details of a new mechanism for the perivascular pump driving glymphatic flow—the brain's waste removal system. The goal was to capture the essence of complex three-dimensional anatomy and physiology of the brain in a reduced order geometric model. The complexity required to make the model even approximately brain-like tended to obscure the most basic features of the perivascular pump. Here a bare-bones, "simplissimo" model of the perivascular pump is presented. It highlights only the most essential features of the pump mechanism. It also reveals components of brain anatomy and physiology that are not strictly necessary to make the pump work. Interestingly, these unnecessary features include pulsatile motion of the vascular walls, pressures inside the arteries and veins within the Virchow-Robin space, differences in arterial and venous compliance, the tapering of vascular branches, and the details of vascular branching. Instead, the softness of surrounding brain tissue and the relative diameters of venous vs. arterial perivascular cuffs are critical. Wave-like deformations of the soft brain tissue can create time averaged positive pressure in periarterial spaces, greater than that in perivenous spaces, owing to differences between antegrade and retrograde resistance to axial fluid flow along the annular channels of Virchow-Robin spaces. This new mechanism is scale independent from mouse to man, and can work despite the widely differing pulse rates of small versus large animals.

Key words. advection, Alzheimer's disease, amyloid, biophysics, blood brain barrier, bulk flow, cerebrospinal fluid, circulation, extracellular, hydraulic, intracranial pressure, perivascular pumping, permeability, pia mater, pulsation, subarachnoid space, Virchow-Robin space, waste.

Introduction

All tissues in the body have a second fluid and solute transport system in addition to the cardiovascular system. Outside the central nervous system, a steady influx of plasma ultrafiltrate through capillaries drives interstitial fluid into tissues, most of which re-enters capillaries at their venular ends. This process by which water and small to medium sized molecules circulate through gaps between capillary endothelial cells is known as Starling's equilibrium of the capillary. Residual tissue fluid that is not returned to the blood stream by the Starling mechanism is drained by lymphatic vessels.

Within the central nervous system, here are no lymphatic channels or lymph nodes. Instead, interstitial fluid is refreshed and waste products are removed by "glymphatic" fluid flow of cerebrospinal fluid through periarteriolar spaces and brain tissue into perivenous spaces. Such fluid flow has been demonstrated experimentally[1], and is considered crucial for removal of waste products, including amyloid beta, a toxic protein that accumulates in Alzheimer's disease[1-3]. However, the mechanism responsible for such apparent interstitial fluid flow remains an open problem[4-9]. The author has proposed a new mechanism[10], demonstrated in a reduced order, geometric model of a human sized cerebral cortex. The present paper focuses on the simplest demonstration of the core mechanism with the fewest necessary components and also extends the mechanism to brains of small laboratory animals.

In the present bare-bones, cartoon like model, the anatomic substrate for the biological perivascular pump, shown in Figure 1(a), is replaced by a single unbranched annular channel, surrounding a rigid cylindrical core representing an artery or vein penetrating the surface of the brain (Figure 1(b)). The core does not move or pulsate. However, companion periarterial and perivenous spaces or cuffs are surrounded by cylinders of soft elastic material, standing in for brain tissue that surrounds the sleeve-like Virchow-Robin spaces. Here the terms Virchow-Robin space and perivascular space (PVS) are used interchangeably. At the brain surface these spaces are continuous with an input reservoir, representing the subarachnoid space. At the other end they are closed. The diameters of the fluid sleeves differ, with veins having roughly twice the sleeve diameters as their companion arteries.

Importantly, the pressure in the subarachnoid space fluctuates in time with the arterial pulse. These fluctuations in intracranial pressure (ICP) are critical for the pump function. They are well known and frequently measured in patients undergoing intracranial pressure monitoring (Figure 2). Identical pressure fluctuations are present at the openings of both periarterial and companion perivenous fluid sleeves. The waveforms and timing of the ICP pulses, shown in Figure 2, suggest that they likely arise from expansion of arteries in the subarachnoid space, which is largely confined within the rigid skull. These changes in intracranial pressure drive cerebrospinal fluid flow in and out of the elastic Virchow-Robin spaces,

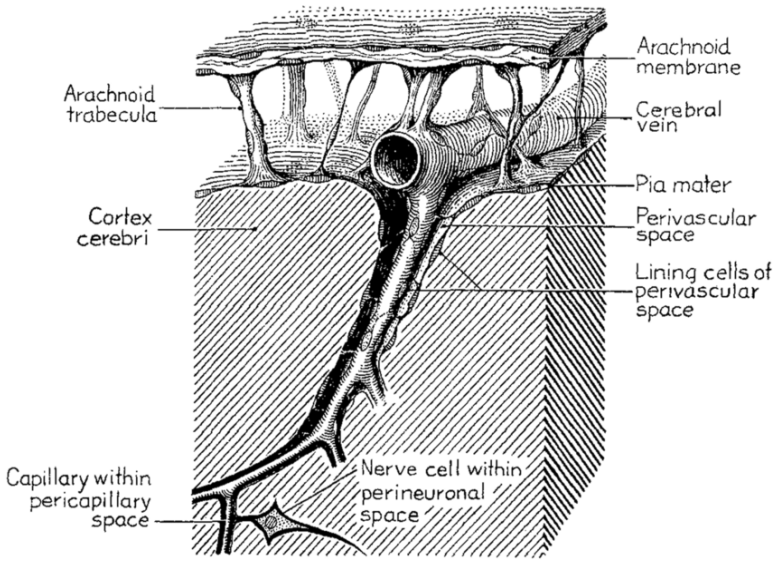

(a)

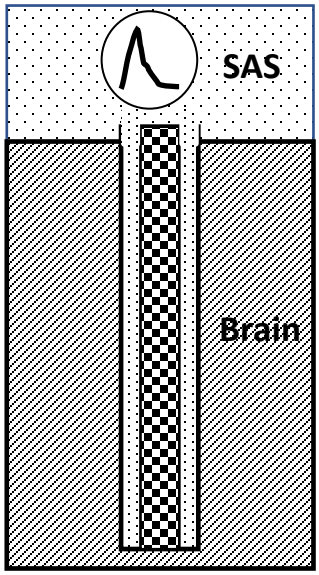

(b)

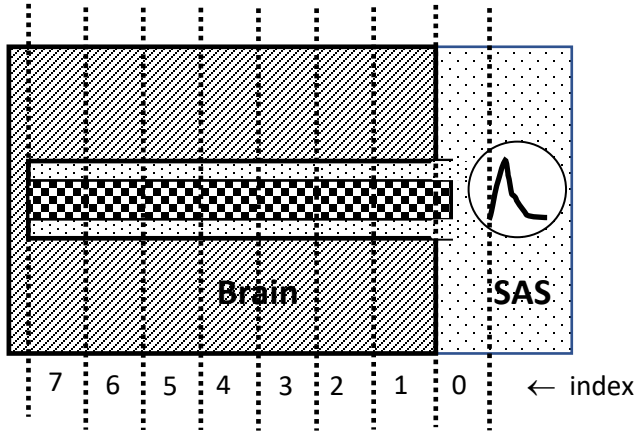

(c)

Figure 1. (a) Relevant anatomy, as drawn by Lawrence Weed in 1923 [11]. (b) Sketch of bare-bones mechanical model; dark checkerboard shading indicates rigid core, light shading indicates cerebrospinal fluid, surrounded by soft elastic brain. SAS denotes subarachnoid space. Changes in intracranial pressure, indicated by the circled waveform in the subarachnoid space, drive fluid flow. (c) Connected slices of discretized model, indexed 0, 1, 2, … according to distance from the subarachnoid space.

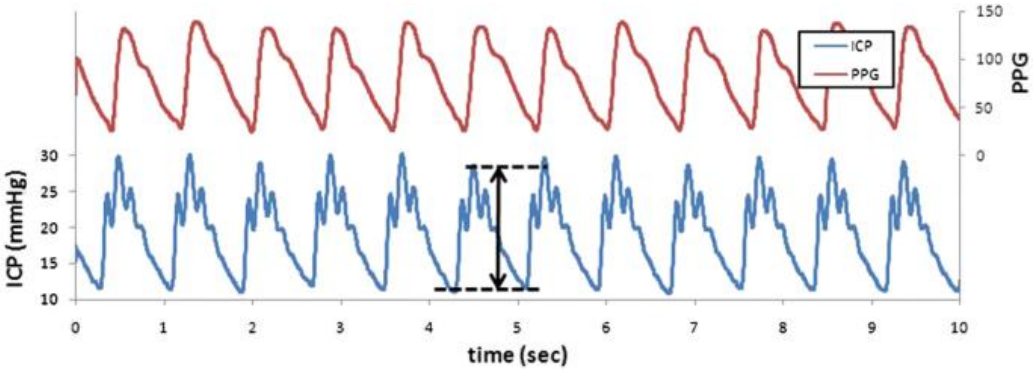

Figure 2. Time domain waveforms of peripheral arterial pulse and intracranial pressure from Evensen[12]. ICP indicates intracranial pressure. PPG indicates photoplethysmogram.

Methods

Discretized model

In Figure 3 the long axis of the perivascular space is horizontal and radial axis is vertical. Axial flow from right to left in the image indicates inflow from the subarachnoid space, deeper into the brain. Flow from left to right indicates outflow into the subarachnoid space. The upper, "north" edge represents the pia covered brain surface. The "south" edge represents the rigid core of the simplissimo model. The dimension in and out of the page is the "hoop" or circumferential dimension. The unstressed diameters are constant; there are no branches.

(a)

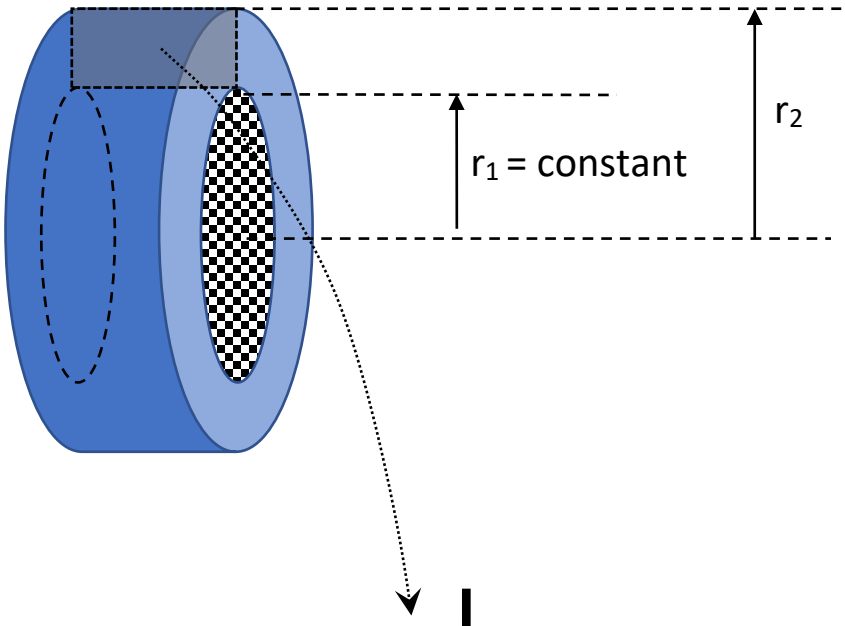
r2
r1 = constant

(b)

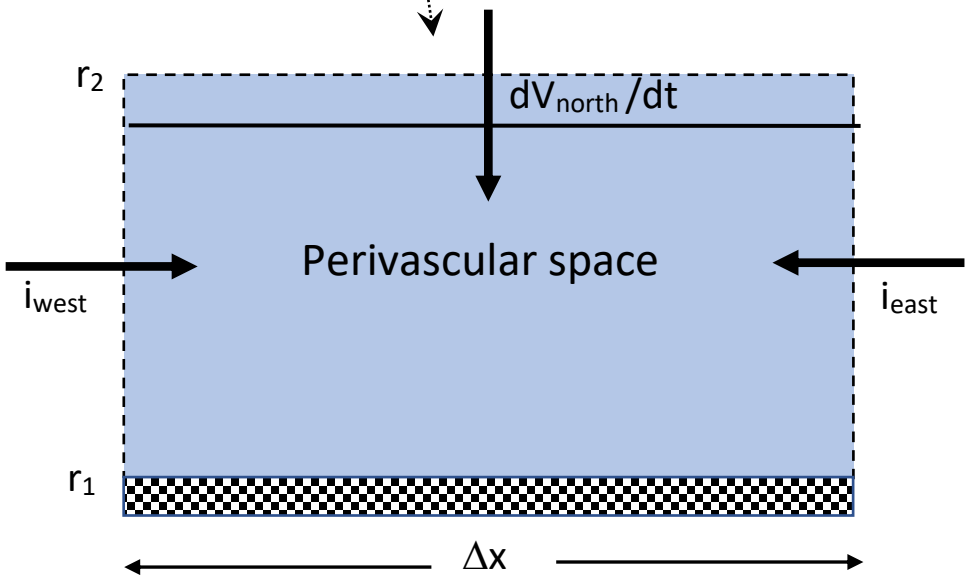
r2
dVnorth /dt
Perivascular space
iwest
ieast
r1
Δx

(c)

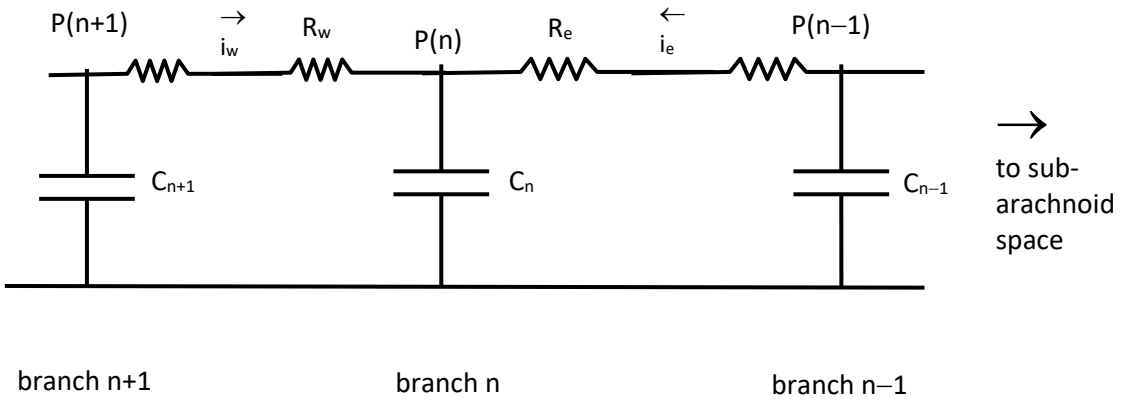

Figure 3. (a, b) Sketches of one segment of the discretized model. Top border represents surrounding brain. Bottom border represents rigid core. Right-left axis is parallel to fluid flow. Positive directions of flows are defined by directions of arrows. dV_{north}/dt represents the effective inflow caused by passive expansion of surrounding brain after prior compression. (c) Sketch of series RC model of fluid flow in perivascular spaces. P denotes pressure. R denotes resistance. C denotes compliance or capacitance. i denotes fluid flow into the indexed segment.

The axial length of the model is divided into multiple segments, Δx long, for the purpose of numerical calculations. Each perivascular segment is surrounded by a cylindrical domain of soft brain tissue, providing a local compliance. The annular space between the brain and the core provides a resistance to axial fluid flow. The model elements are connected in a series resistive-capacitive (RC) arrangement to create a reduced order model of axial fluid flow (Figure 3(c)) similar to those commonly used in cardiovascular physiology[13]. Radius r_1 represents the constant radius of the rigid core, substituting for an artery or vein. Radius r_2 represents the radius of the extended Virchow-Robin space. Radius r_3 represents the outer radius of the surrounding cylinder of soft brain tissue, where $r_3 > 10\ r_2$.

Changes in perivascular volumes and pressures

Consider first a brain penetrating artery surrounded by its perivascular cuff. Radial directions correspond to the north--south direction, and axial directions correspond to the east--west direction in Figure 3. CSF can flow along the right-left, or east-west axis of the perivascular space from one discrete segment to another. These flows are denoted as i_{east} and i_{west} in Figure 3, with signed directions denoted by the arrows. In addition, using the sign conventions in Figure 3(b), downward expansion of surrounding elastic brain tissue in response to a negative change in

cuff pressure would cause an effective inflow, $i_{north} = dV_{north}/dt > 0$ in time increment, dt. Upward compression of surrounding elastic brain tissue in response to a positive change in cuff pressure would cause an effective outflow $i_{north} = dV_{north}/dt < 0$. If all signed inflow values sum to zero (that is, net inflow equals net outflow) then the compartmental volume is constant. Zero volume change occurs from the south side, because in this special case the core, standing in for a blood vessel, is rigid for the sake of maximal simplicity.

Typically, the volume of perivascular fluid will change due to resistive axial flows during time increment, dt . Let the combined Poiseuille resistance to flow from the right be denoted R_{in} and the combined Poiseuille resistance to flow from the left be denoted R_{out} . For indexed segment, n, let the neighboring segmental pressures, P , be indexed n – 1 on the input side toward the subarachnoid space, and n + 1 on the output side toward the center of the brain. Then

$$dV_{east} = i_{east}dt = \frac{P_{n-1} - P_n}{R_{east}}dt \ , \tag{1}$$

and similarly,

$$dV_{west} = i_{west}dt = \frac{P_{n+1} - P_n}{R_{west}}dt \ . \tag{2}$$

If there is a net inflow minus outflow, together with expansion or contraction of the surrounding brain tissue, then in time increment, dt, the volume of the segment will change by amount

$$dV_{pvs} = dV_{east} + dV_{west} - C_{brain}dP_{pvs} \ , \tag{3}$$

and the pressure in perivascular space will change by amount

$$dP_{pvs} = \frac{dV_{pvs}}{C_{brain}} = \frac{dV_{east} + dV_{west} - C_{brain}dP_{pvs}}{C_{brain}} \ . \tag{4a}$$

Now solving for the change in pressure,

$$dP_{pvs} = \frac{dV_{east} + dV_{west}}{2\ C_{brain}} \ . \tag{4b}$$

Then local perivascular volumes and pressures can be dynamically updated each time step,

$$V_{pvs} = V_{pvs} + dV_{pvs} \ . \tag{5}$$

$$P_{pvs} = P_{pvs} + dP_{pvs} \ . \tag{6}$$

Also, for cylindrical sectors, noting that core vascular volume in this simplified model is $\pi r_1^2 \Delta x$ and that $\pi r_1^2 \Delta x \ + V_{pvs} = \pi r_2^2 \Delta x$, one can also update values of cuff radius

$$r_2 = \sqrt{\frac{\pi r_1^2 \Delta x + V_{pvs}}{\pi \Delta x}} \tag{7}$$

with r_1 and r_2 being larger for veins than for arteries.

Resistance of segmental perivascular spaces to axial fluid flow

To calculate resistance, imagine the perivascular space as being split longitudinally and opened to form a flat sheet with a width equal to the average radius, $2\pi(r_1+r_2)/2$, and a thickness of $r_2 - r_1$. Classically[5], for flow of a fluid having viscosity, μ , between two parallel plates of width $2\pi(r_1+r_2)/2$, length Δx, and separation $r_2 - r_1$, we have axial resistance of the perivascular space

$$R \approx \frac{12\mu\Delta x}{2\pi\frac{(r_1+r_2)}{2}(r_2-r_1)^3} = \frac{12\mu\Delta x}{\pi(r_2+r_1)(r_2-r_1)^3} . \tag{8}$$

This is a reasonable approximation to the resistance to axial flow in the cuff of fluid forming the perivascular space. To include instantaneous changes in this nonlinear axial resistance, R, it is necessary to account for small, time-varying changes in the arterial and perivascular radii, which must be recomputed each time step, dt. Then, to calculate axial resistance between perivascular cuffs of different branches, one can compute interface resistance as series combination of upstream and downstream half segments

$$R_{east}(n) \approx \frac{1}{2}(R_{n-1} + R_n) \tag{9}$$

and

$$R_{west}(n) \approx \frac{1}{2}(R_n + R_{n+1}) . \tag{10}$$

Compliance of surrounding brain tissue

As shown in the Appendix, it is easy to demonstrate from basic mechanical principles that the constant compliance, C_{brain} , of a cylindrical segment of surrounding brain tissue in Figure 3 is given by the expression

$$C_{brain} = \frac{2\pi r_2^2 \Delta x}{E} ln\left(\frac{r_3}{r_2}\right), \tag{11}$$

where E represents Young's modulus of stiffness for brain tissue[14], and ln() represents the natural logarithm. Here for simplicity the ratio $r_3/r_2 = 12$ in all simulations.

Scale independence

From inspection of Equation (8) one can see that for similar shaped annular channels having constant length to width ratio, represented by $\Delta x/r_2$, that 1/R is proportional to r_2^3 or volume. Hence from Equations (1) and (2) dV_{east} and dV_{west} are also proportional to r_2^3 . Equation (11) shows that for similar length/width channels, C_{brain} is also proportional to r_2^3 . Hence, changes in pressure from Equation (4b), namely $dP_{pvs} = \frac{dV_{east}+dV_{west}}{2\,C_{brain}}$, are proportional to $\frac{r_2^3}{r_2^3} = 1$ and are scale independent. The resulting pump pressures should scale, in a general sense, from mouse to man.

Numerical values of model parameters

Table 1 presents specific numerical values of input parameters of a standard normal model.

Table 1. Standard Model Parameters

Symbol	Definition	Value	Units
PVratio	Perivascular space to core vessel ratio (r_2/r_1)	2	
VAratio	Venous to arterial model diameter ratio	2	
dt	Time increment for numerical integration	0.0001	sec
Freq	Cardiac frequency or pulse rate	1	Hz
Δx	Length of perivascular segment	0.5--1	cm
μ	Viscosity of cerebrospinal fluid	0.01	dyne/cm^2-sec
E_{brain}	Young's modulus of brain tissue	10000	dyne/cm^2
N	Number of discrete segments in model	10--20	
π	Circle ratio	3.1416	
ΔP_{max}^{sas}	One half pulse pressure in subarachnoid space CSF	2	mmHg
r_1	Radius of rigid core	0.03	cm
r3_r2	Ratio of outer soft tissue radius to PVS radius	12	

Numerical methods

Code is written in Microsoft Visual Basic and executed on an ordinary laptop computer. Pressures, volumes, axial resistances for a particular vascular domain, either arterial or venous, are computed iteratively for successive small time steps, dt = 0.0001 sec, from "cold start" initial conditions (mean ICP in all compartments) until the pulsatile pressure changes and the time averaged pressure differences become cyclically stable, reaching a steady-state (> 30 sec). Pulsatile changes in arterial pressure and similar pulsatile changes from mean ICP are computed using approximate arterial pulse waveforms

$$\Delta P(t) = \Delta P_{max}\left[(sin\,(\omega t) + \tfrac{1}{2}(sin\,(2\omega t))\right]. \qquad (12)$$

For intracranial pressure pulses in the subarachnoid space $\Delta P_{max} = \Delta P_{max}^{sas}$ (2 mmHg in the standard model, representing 4 mmHg peak-to-peak). The standard simulation duration is 40 seconds, after which cyclic pressures and volumes become clearly stable. In real time each arterial or venous pressure simulation requires about 10 seconds to execute. The core algorithm for numerical integration of model variables can be outlined as follows:

COMPUTATIONAL ALGORITHM

```
Initialize variables

For each time step, dt {
    Compute time varying ΔICP [Eq. 12]

    For each segment, n , compute {
       dVeast [Eq. 1]
       dVwest [Eq. 2]
       dPpvs [Eqs. 4(b), 11]
       dVpvs [Eq. 3]
       Vpvs = Vpvs + dVpvs [Eq. 5]
       Ppvs = Ppvs + dPpvs [Eq. 6]
       r2 [Eq. 7]
       Rpvs(n) [Eq. 8]
    }

}
```

Typical outputs include perivascular pressures, volumes, and radii.

Results

Mechanical action of the pump

Figure 4 illustrates snapshots of arterial and venous perivascular space pressures for the standard model of Figure 1 during a steady state pressure cycle. Figure 5 illustrates corresponding snapshots of arterial and venous perivascular radii. Graphs from top to bottom indicate pressures in periarterial spaces (left) and perivenous spaces (right) as a function of axial distance from the SAS in cm. Since pulse rate is 1 Hz, these sample times also represent 0, 25 50, and 75 percent of the pulse period. At most sample times there is a positive periarterial minus perivenous pressure difference. A hint of wave like action is present, but the wave is propagating through the outer wall of brain tissue. It is not propagating through the wall of the core blood vessel, which is rigid.

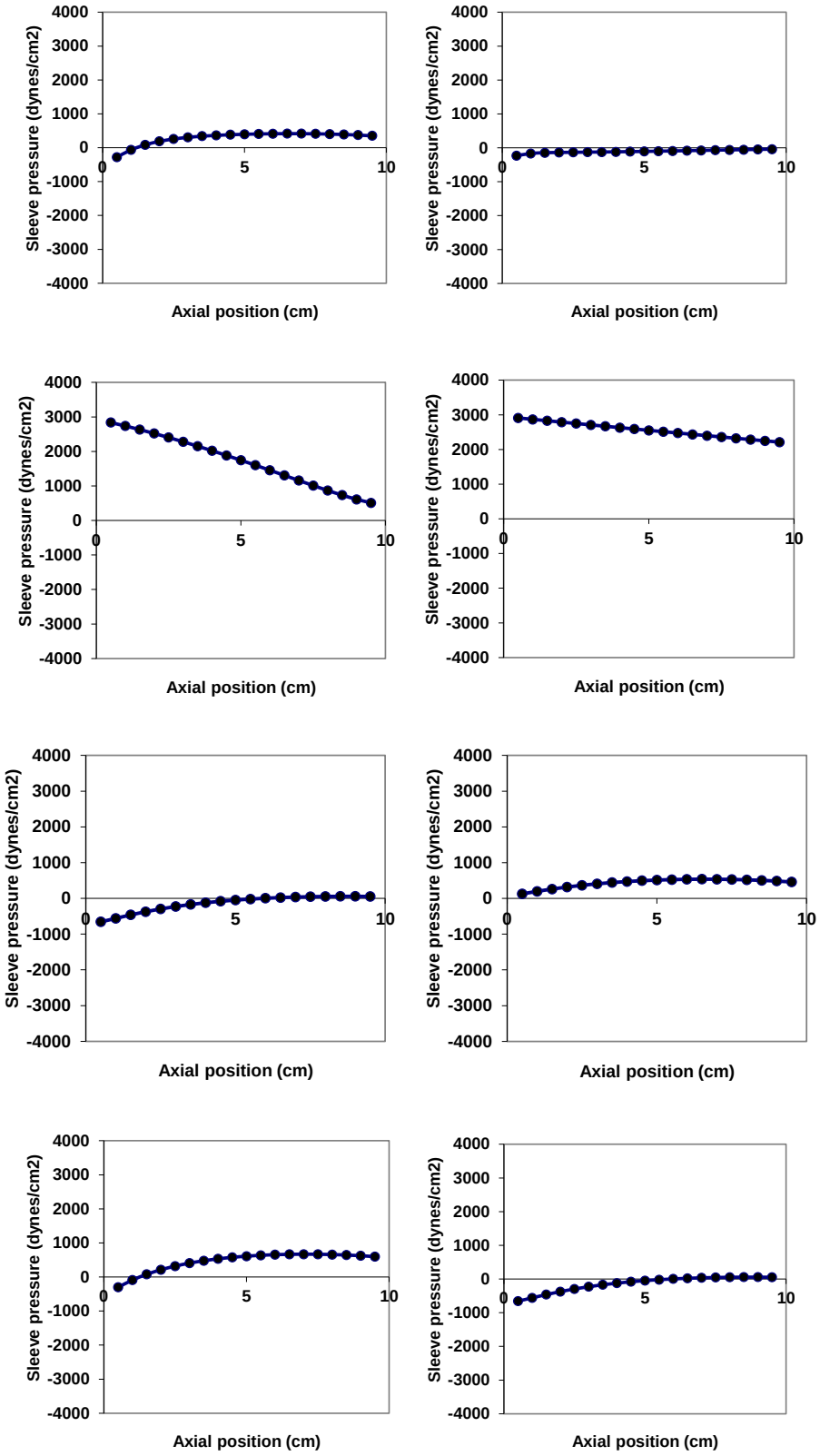

Figure 4. Pressures (top to bottom) at 0, 0.25, 0.5 and 0.75 sec in periarterial spaces (left) and perivenous spaces (right).

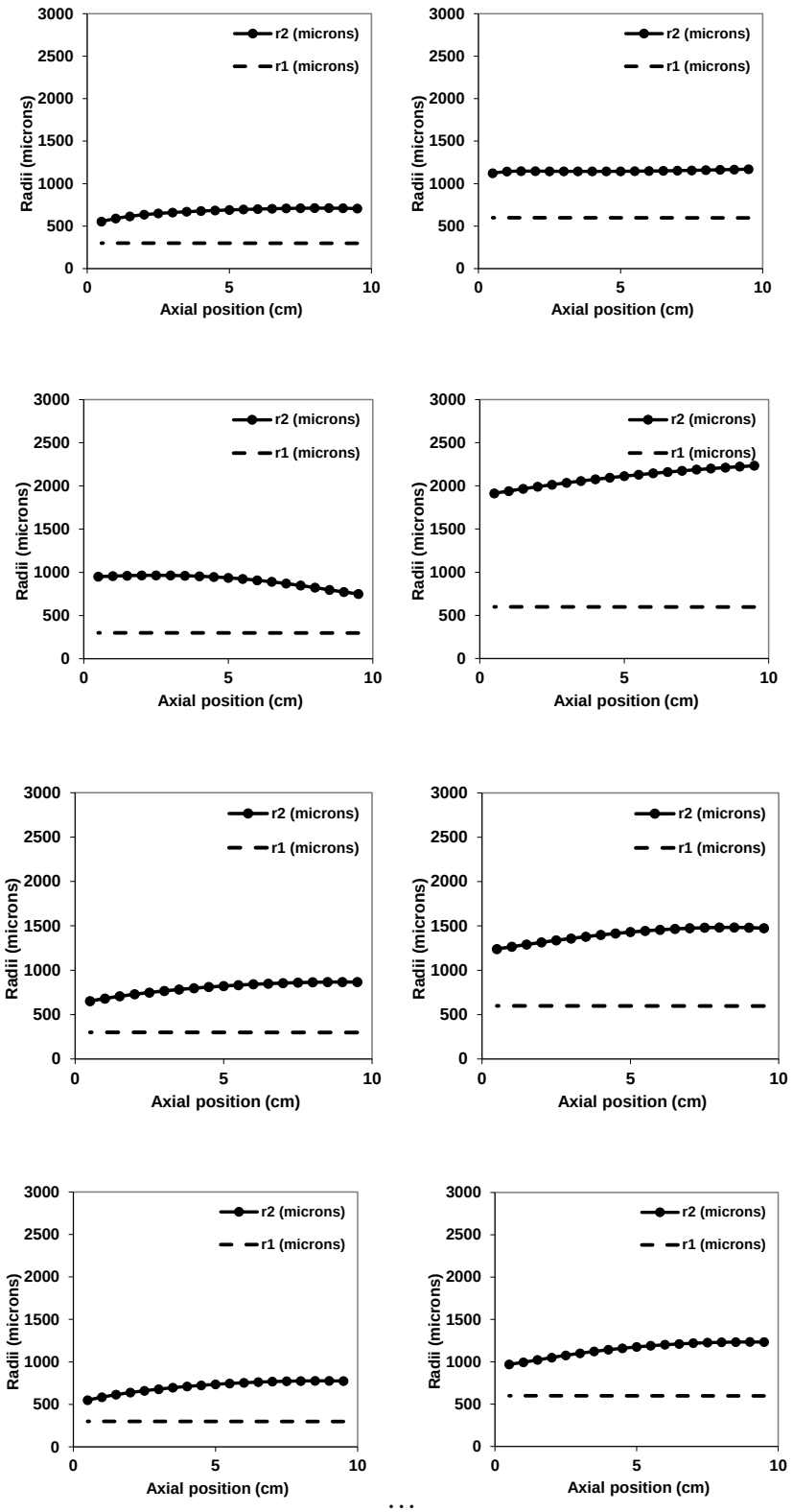

...

Figure 5. Radii (top to bottom) at 0, 0.25, 0.5 and 0.75 sec in periarterial spaces (left) and perivenous spaces (right).

Time domain waveforms of periarterial and perivenous resistances

One clue to the underlying mechanism of the perivascular pump is revealed by time domain plots of periarterial resistance to axial, or east-west fluid flow.

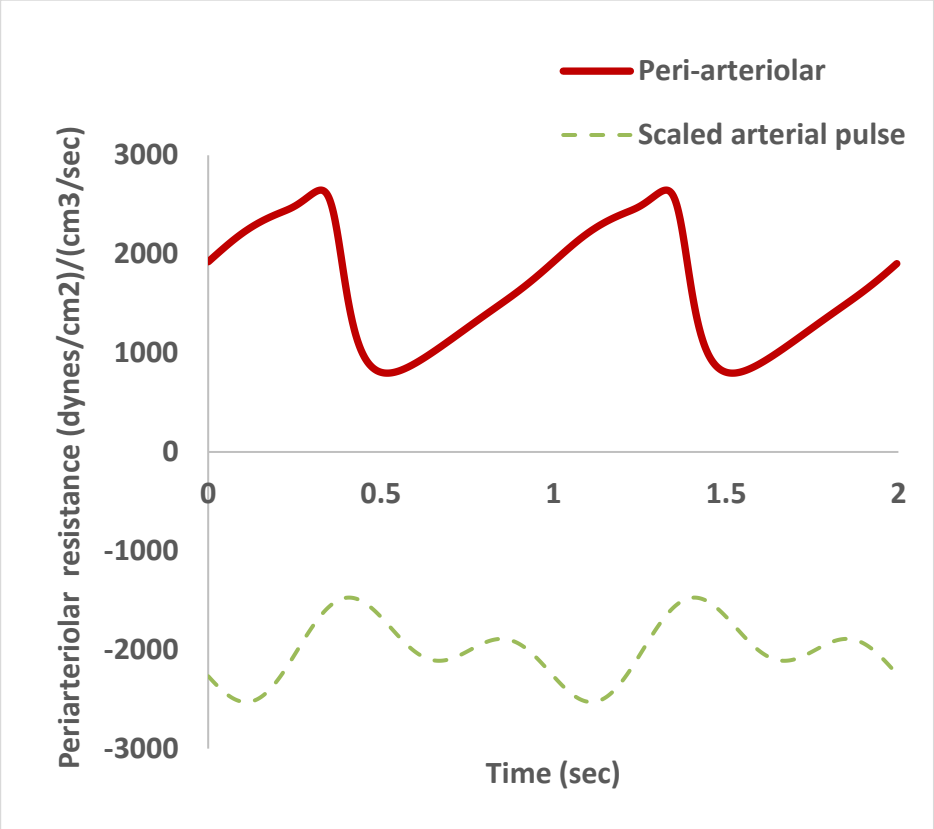

Figure 6. Time domain tracings of periarterial axial resistance in a middle segment of the model of Figure (3) after 40 sec of steady pumping. Dashed curve represents scaled intracranial pulse waveform as a timing reference. The slight delay in onset of resistance changes is caused by pulse propagation in the expanding soft walled perivascular channels.

As shown in Figure 6, during the channel filling phase (inflow) periarterial axial resistance falls as channel width increases. During the channel emptying phase (outflow) periarterial axial resistance rises. The difference in inflow vs. outflow resistance creates a partial valve or diode that tends to trap fluid in the periarterial space, causing a positive average pressure. The narrowed channel seems to slow outflow back into the subarachnoid space between pulses. Narrower periarterial channels slow flow more than wider perivenous channels, allowing a time-averaged perivascular pressure difference to develop.

Time domain waveforms of arterial and intracranial pressures

Figure 7 shows the time domain pressure waveforms in companion peri-arterial and peri-venous spaces of the unbranched model in Figure 3 as fluid flows in and out of Virchow-Robin spaces in response to cyclic changes in ICP. On the arterial side, the narrowed channel seems to slow outflow back into the subarachnoid space between pulses more than on the venous side, allowing the time-averaged perivascular pressure difference to persist.

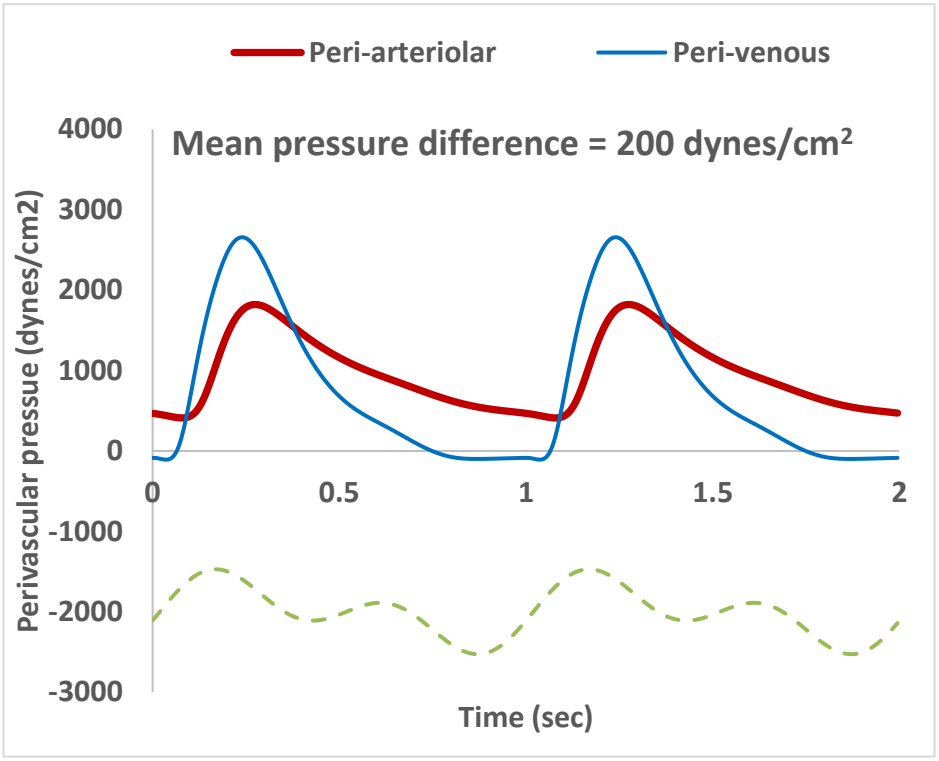

Figure 7. Periarterial and perivenous pressure tracings after 40 sec of steady pumping. Dashed curve represents scaled intracranial pulse waveform as a timing reference.

Figure 8 illustrates time domain waveforms of vascular and perivascular radii. Radii r_1 represent the fixed diameter rigid cores, and radii r_2 represent the CSF filled Virchow-Robin spaces.

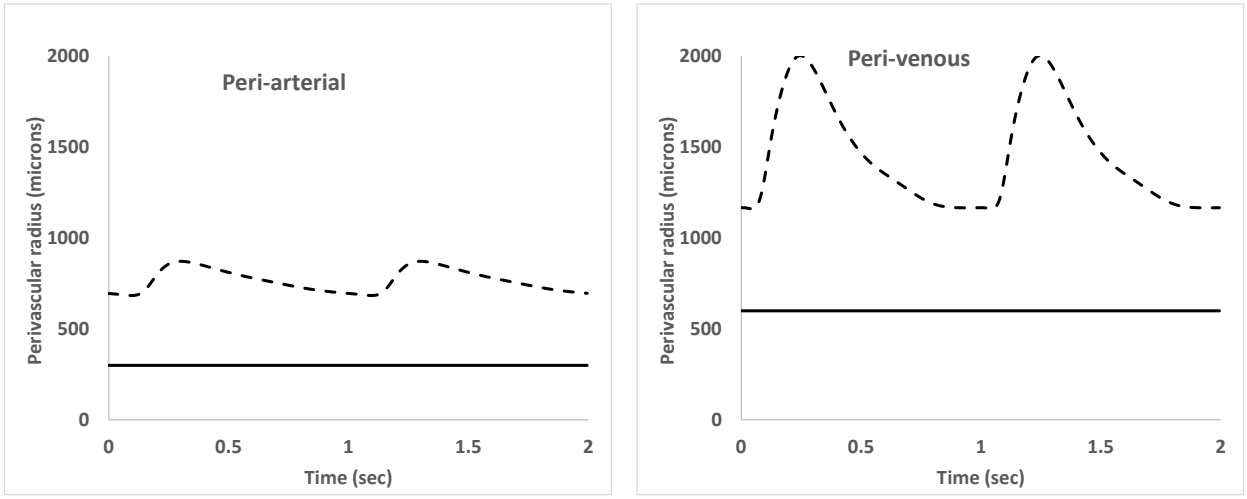

(a) (b)

Figure 8. Time domain waveforms of perivascular (r_2) and constant core (r_1) radii illustrating a pumping mechanism independent of core pulsations. Cuff width, $r_2 - r_1$, is smaller around arteries (a) than around veins (b).

The arterial radii (a) are less than the venous radii (b), accounting for higher resistances to axial flow in (a). The outer walls of the perivascular spaces having radii r_2 (dashed curves) expand according of the compliance of the channel through soft brain tissue. There is a relatively greater net expansion of the perivenous space in response to fluid inflow from the subarachnoid space.

Time averaged perivascular pressure gradients

Figure 9 shows differences between mean pressure inside the perivascular spaces surrounding arteries and mean pressure inside the perivascular spaces surrounding companion veins, plotted as a function of axial distance from the SAS. The differences are greater in segments closer to the pressure source than in more distal segments. These spaces have arteries 300 microns in radius and companion veins 600 microns in radius.

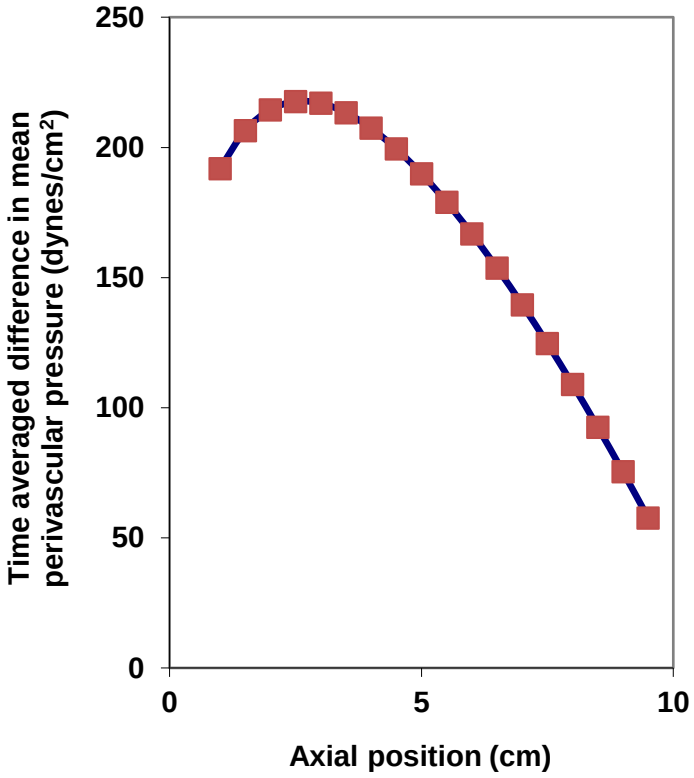

Figure 9. Time averaged pressure differences in dynes/cm^2 between periarterial and perivenous spaces as a function of axial distance from the pressure source in the subarachnoid space.

Figure 10 shows steady-state perivascular arteriovenous, or AV, pressure differences between a 300-micron radius artery model and 600-micron radius vein model at a middle axial distance (5 cm) as a function of variable perivascular space width, quantified as the cuff ratio. The cuff ratio is defined as the radius of the perivascular space divided by the radius of the local artery or vein. A cuff ratio of 1.00 would indicate a zero-width perivascular space. In the standard normal model, the cuff ratio is 2.0. The generation of a positive AV perivascular difference is dependent on a relatively narrow perivascular space width and a relatively small cuff ratio.

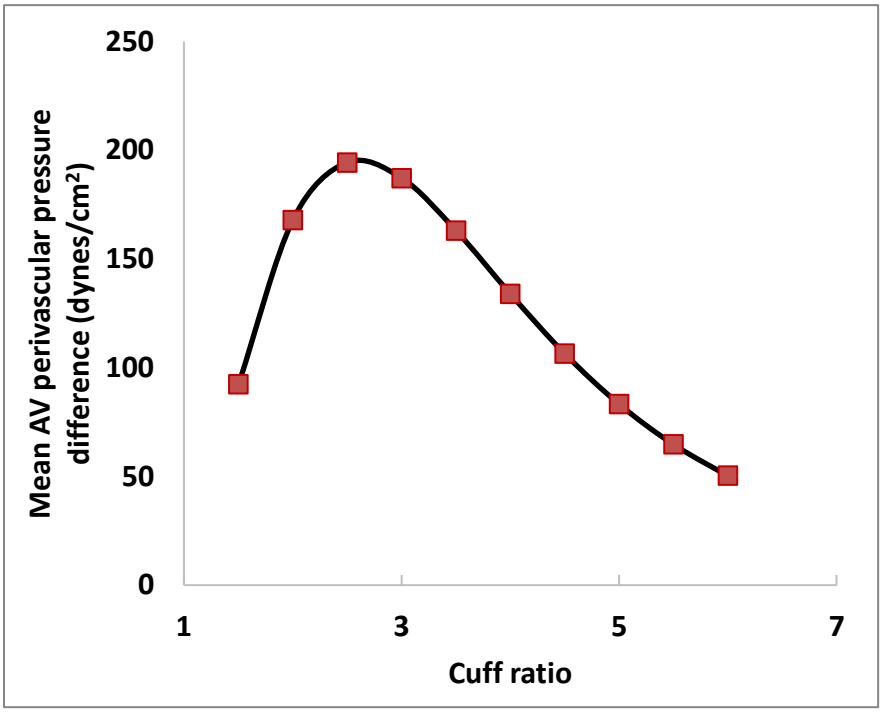

Figure 10. Mean periarterial minus perivenous pressures as a function of the cuff ratio, defined as the radius of the perivascular space to the radius of the local artery or vein. A cuff ratio of 1.00 would indicate a zero-width perivascular space. A cuff ratio of 2 is roughly normal. AV denotes arteriovenous.

Figure 11 shows steady-state perivascular arteriovenous, pressure differences in the otherwise standard model of Figure 8 as a function of the peak-to-peak intracranial pulse pressure for various cuff ratios. Each curve represents a different peak-to-peak amplitude of intracranial pressure in the subarachnoid space. As the driving pressure pulses increase in amplitude from bottom to top curves, the positive differences in perivascular pressure between companion periarteriolar and perivenular spaces become greater in an almost linear way, consistent with the idea that ICP pressure pulses provide the driving forces for the perivascular pump.

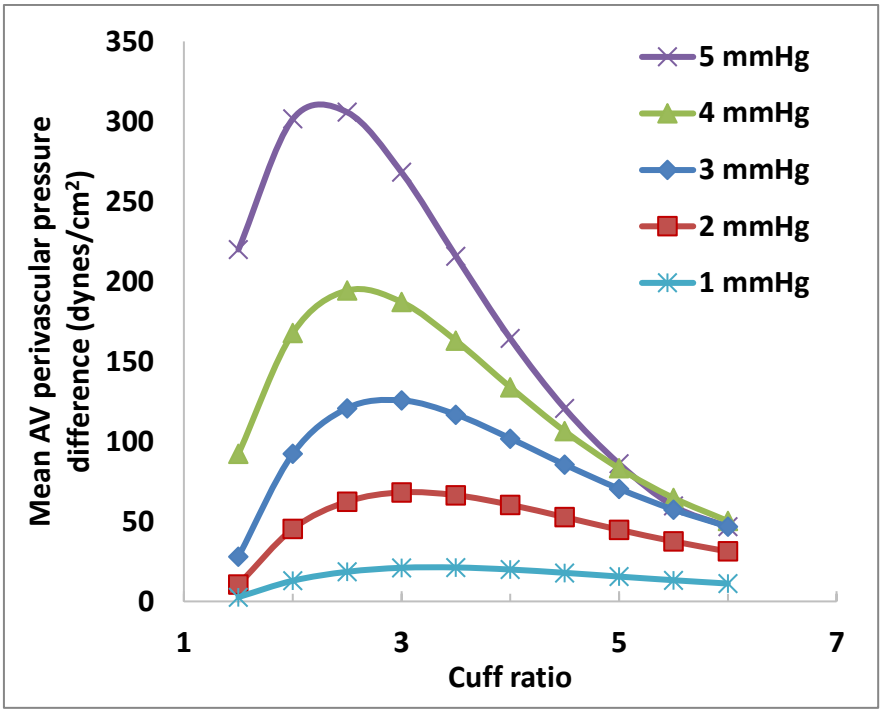

Figure 11. Mean periarterial minus perivenous pressures as a function of Cuff ratio and peak-to-peak ICP fluctuations in mmHg, indicated in the figure legend.

Figure 12 shows steady-state perivascular arteriovenous pressure differences in the otherwise standard model of Figure 7 as a function of the cuff ratio for various vein/artery (V/A) diameter ratios. Each curve represents a different size difference between veins and their surrounding perivascular spaces and arteries and their surrounding perivascular spaces. For an VA ratio of 2, for example, both veins and perivenous spaces are twice the diameter of companion arteries and periarterial spaces. For a VA ratio of 1, the veins and arteries are identical. As seen in Figure 9, when the VA ratio equals one, there is no pressure difference between periarterial and perivenous spaces, since the vessels are identical. As the VA ratio increases from bottom to top curves, the positive differences become greater. Positive differences are also dependent on the cuff ratio in a curvilinear way. In these simulations the amplitudes of the SAS pressure pulses are the same.

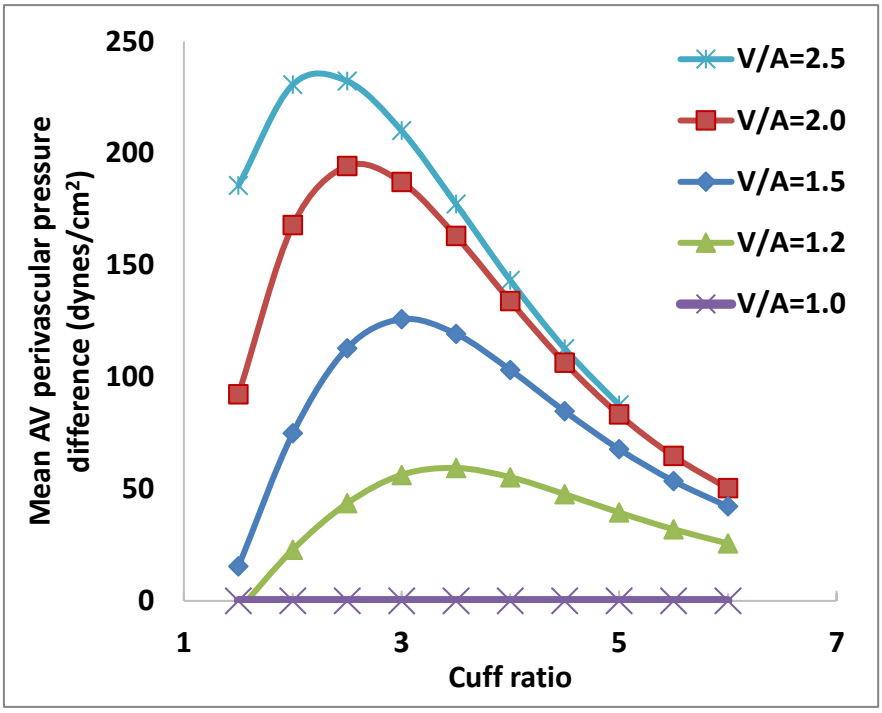

Figure 12. Mean periarterial minus perivenous pressures as a function of Cuff ratio and vein to artery (V/A) diameter ratio.

Figure 13 shows steady-state perivascular arteriovenous, pressure differences in the otherwise standard model of Figure 7 as a function of the cuff ratio at various heart rates. Each curve represents a different heart rate, or pulse repetition frequency. For cuff ratios less than 3, slower heart rates produce greater mean AV perivascular pressure differences capable of driving glymphatic fluid flow.

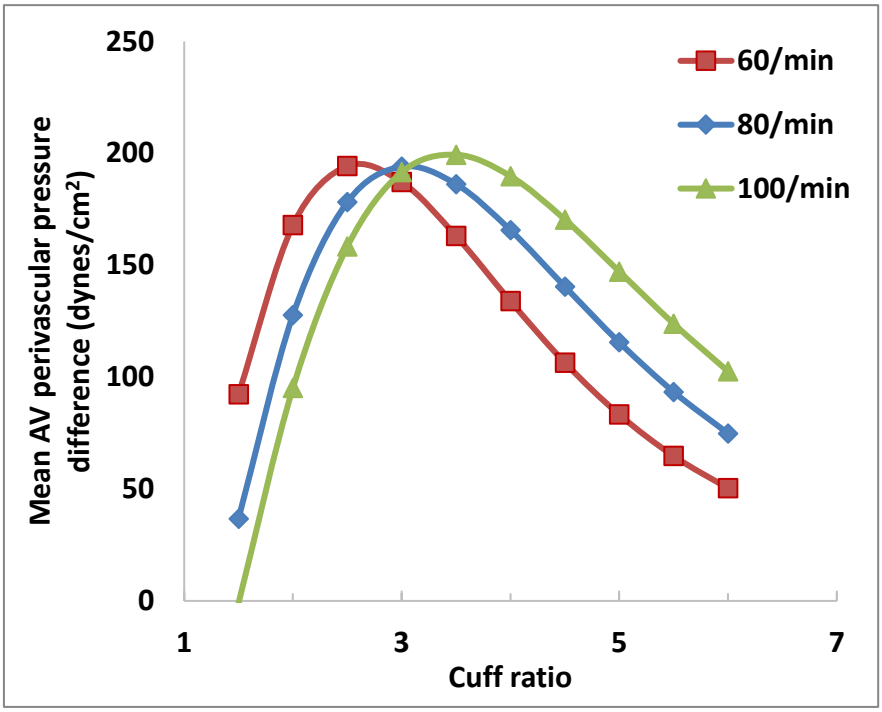

Figure 13. Mean periarterial minus perivenous pressures for the standard VA ratio = 2 as a function of Cuff ratio and heart rate.

The heart rate paradox

It appears from Figure 13 that the AV interstitial fluid pressure difference is dependent in an interesting way upon heart rate as well as cuff ratio. To explore this phenomenon further, a scan of various heart rates was performed in the otherwise standard model, having a total axial length of 10 cm.

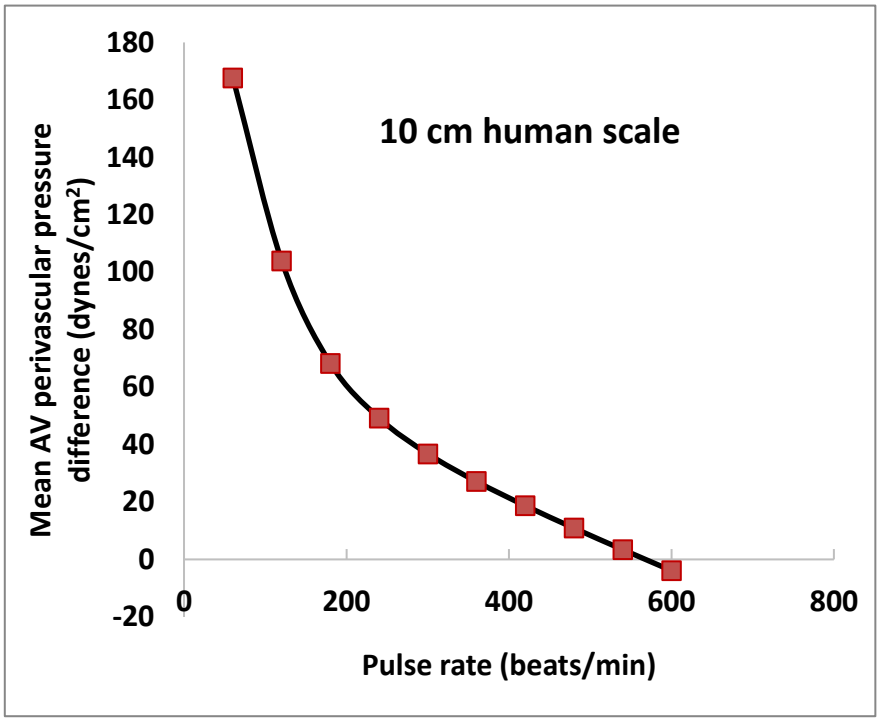

Figure 14. Effects of ICP pressure pulse rate or heart rate in beats/min upon mean AV perivascular pressure difference.

Figure 14 shows that the presumptive pressure difference driving bulk flow of interstitial fluid is heart rate dependent in the human scale model. In keeping with expected biological effects, this result means that interstitial fluid flow would be greater during sleep in humans with lower sleeping than awake heart rates. This result also, however, brings up a paradox. If the simulated pump mechanism is indeed scale independent, then a small rodent with a much faster pulse rate than a human would have much less effective brain waste removal via the proposed pump mechanism.

Resolution of the paradox can be done by creating a more realistic rodent model. The arteries on the surface of a mouse brain are much smaller in diameter than the corresponding arteries of a human brain. Yet the capillaries and end arteries are the same diameter in both species. Fewer branches are needed in a rodent. The total length from brain surface to terminal arteriolar branches is much less. Figure 15 shows results for a small brain model in which the artery radius

is reduced from 300 microns to 100 microns in keeping with real anatomy. The companion vein diameter is reduced from 600 microns to 300 microns. The total axial lengths of both arteries and veins are reduced relatively more--from 10 cm to 1.2 cm. In this revised and highly simplified rodent model the heart rate effect is substantially modified. The curve of AV pressure difference is shifted toward the right. The values at rat or mouse like heart rates, in the range of 400 to 600 per minute, are similar to those in the larger human model. Further, the downward slope in this range indicates that interstitial fluid flow and brain waste clearance would be improved at lower sleeping heart rates than at awake active heart rates in rodents. If this representation is indeed correct, that is, in going from man to mouse there is relatively greater shrinking in arteriolar length than in arteriolar diameter, then the heart rate paradox can be resolved.

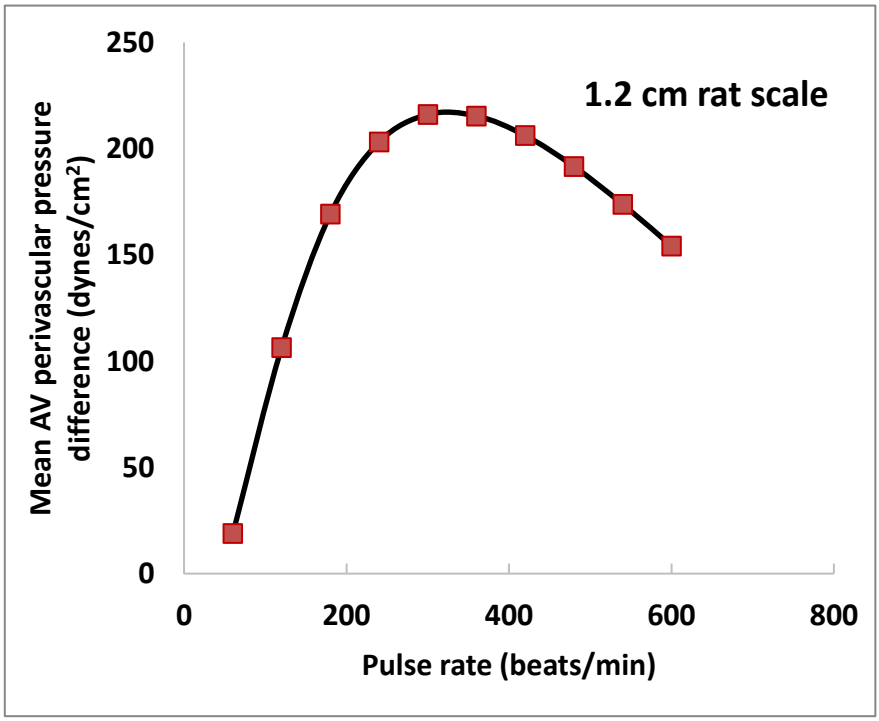

Figure 15. Effects of ICP pressure pulse rate or heart rate in beats/min upon mean AV perivascular pressure difference.

Discussion

This paper describes a reduced order mechanical model to elucidate a possible overlooked physical mechanism driving glymphatic fluid flow. Positive perivascular pressure differences can be demonstrated in a highly simplified model, in which the driving force is provided, not by arterial blood pressure fluctuations, but rather intracranial pressure fluctuations synchronized with the arterial pulse. Waves of radial stretch propagate, not in blood vessel walls, but rather in soft brain tissue surrounding the Virchow-Robin spaces. The velocity of pulse wave propagation in soft walled channels of brain tissue surrounding perivascular spaces is much less than that in arteries, which have greater than 10 times the stiffness (Young's modulus) of brain tissue. In addition, the local microscopic architecture of the blood brain barrier and the presence of astrocytic processes and end-feet[1,11,15] may further reduce the stiffness of a thin layer of brain tissue immediately bordering the Virchow-Robin spaces.

Importantly, the present model does NOT simulate peristaltic pumping of arterial walls, as has been suggested[16]. Arterial pulsations within the Virchow-Robin space are not required. Instead, intracranial pressure pulses created by expansion of large arteries in the subarachnoid space make the pump work. The present results suggest that the creation of time averaged positive pressures in Virchow-Robin spaces happens in response to time varying axial resistances to fluid flow, with inflow resistances during systole being less than outflow resistances during diastole.

A clinical analog can be found in a patient with moderate aortic valve insufficiency, also called aortic regurgitation. Normally the aortic valve has very low resistance to blood flow during systolic ejection from the left ventricle, but very high, essentially infinite, resistance to backflow out of the aorta after the valve closes in diastole. In a patient with aortic valve insufficiency the backflow resistance is finite, allowing substantial regurgitation of blood back into the left ventricle. Still, forward resistance is less than backward resistance, and the patient is able to retain some positive diastolic pressure in the aorta and remain alive until corrective surgery. A difference between inflow and outflow resistance can act as a leaky, but partially effective, valve, because there is more resistance to retrograde flow than to antegrade flow.

Kedarasetti, Drew, and Costanzo[17] at Pennsylvania State University showed that peristaltic arterial pulsations can drive oscillatory flow of CSF but not directional pumping. In 3D fluid dynamics simulations, driven by arterial wall movement within an elliptical perivascular space, they found no inherent preference to directional flow in the perivascular space. However, in keeping with the present model and concept, Kazimierska et al.[18] suggested the importance of elasticity of the brain tissue surrounding perivascular spaces. They viewed the brain as a porous medium that is soft enough to be deformed appreciably by the pressures squeezing fluid through pores, and they concluded that further study of poroelastic pumping is warranted. Here, the present analysis shows that wave-like deformation of blood vessels is not required at all for perivascular flow. However, wave-like deformation of the soft brain in the surrounding perivascular space is essential. In this case a positive pressure difference, capable of driving biological meaningful poroelastic bulk flow[10] can develop, owing to differences between antegrade and retrograde resistance to axial fluid flow along the annular channels of Virchow-Robin spaces.

Appendix: compliance of a brain domain

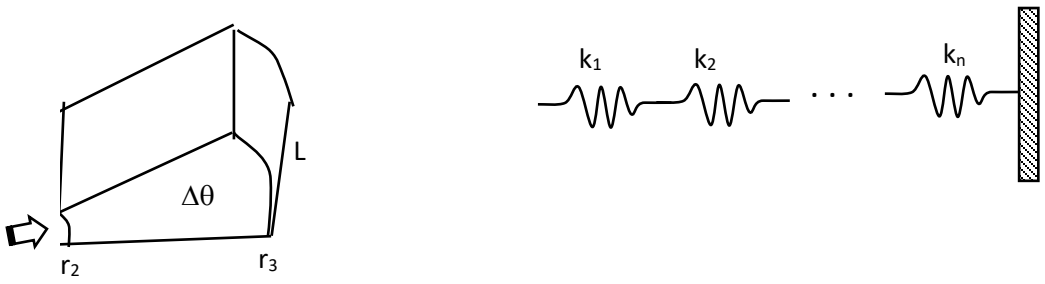

(a) (b)

Figure 15. Compression of wedge-shaped sector of an elastic cylinder.

Figure 15 (a) shows a wedge-shaped section of a cylindrical brain domain of angle $\Delta\theta$. Radius, r_2 , represents the outer border of the perivascular space. Ordinary brain tissue fills the wedge shape from r_2 to r_3 . To appreciate the elastic properties of this composite structure, consider multiple radial layers of brain, dr thick, as constituting series springs as shown in (b). The series springs are characterized by spring constants, k_1 , k_2 , and so on. Quantitatively, the reactive force produced by compression of the stacked springs in Figure 15 (b) by total amount, Δx , is given by $F = k_{total}\,\Delta x$, where the combined spring constant, k_{total} , of the series springs is classically given by the expression

$$\frac{1}{k_{total}} = \frac{1}{k_1} + \frac{1}{k_2} + \cdots + \frac{1}{k_n}\,. \tag{A7}$$

For a rectangular elastic solid of surface area A, thickness, h, and Young's modulus of stiffness, E , the effective spring constant is given by the formula, k = "EA/h". Young's modulus is a known material property of brain tissue (~ 1 kPa). Hence, by calculus, we can write

$$\frac{1}{k_{total}} = \int_{r_2}^{r_3} \frac{dr}{ELr\Delta\theta} = \frac{1}{EL\Delta\theta}\int_{r_2}^{r_3} \frac{1}{r}\,dr = \frac{1}{EL\Delta\theta}\,ln\left(\frac{r_3}{r_2}\right). \tag{A8}$$

Inverting Equation A8, the lumped spring constant of the stacked layers of ordinary brain tissue in one cylindrical domain

$$k_{total} = \Delta\theta\,\frac{E_{brain}\,L}{\ln\left(\frac{r_3}{r_2}\right)}\,. \tag{A9}$$

The reactive pressure from expansion of the perivascular space of radius r_2 equals the reactive force divided by area, $k_{total} * \Delta r_2$ / surface area or

$$\Delta P = \frac{k_{total}\Delta r_2}{r_2 \Delta\theta L} = \Delta\theta \frac{E_{brain}\, L}{\ln\left(\frac{r_3}{r_2}\right)} \frac{\Delta r_2}{r_2 \Delta\theta L} = \frac{E_{brain}}{\ln\left(\frac{r_3}{r_2}\right)} \frac{\Delta r_2}{r_2} . \quad \text{(A10)}$$

The compliance of the sector of brain tissue is the incremental change in volume divided by the incremental change in pressure

$$C = \frac{\Delta V}{\Delta P} = \frac{r_2\, \Delta\theta L \Delta r_2}{\frac{E_{brain}\, \Delta r_2}{\ln\left(\frac{r_3}{r_2}\right)\, r_2}} = \frac{r_2^2\, \Delta\theta L}{E_{brain}} \ln\left(\frac{r_3}{r_2}\right) . \quad \text{(A11)}$$

For the full circular cross section, the compliance is

$$C = \frac{2\pi r_2^2\, L}{E_{brain}} \ln\left(\frac{r_3}{r_2}\right) . \quad \text{(A12)}$$

References

1. Kelley D, Thomas J (2023) Cerebrospinal Fluid Flow. Annual Review of Fluid Mechanics 55: 237-264.
2. Iliff JJ, Wang M, Liao Y, Plogg BA, Peng W, et al. (2012) A paravascular pathway facilitates CSF flow through the brain parenchyma and the clearance of interstitial solutes, including amyloid beta. Sci Transl Med 4: 147ra111.
3. Rasmussen MK, Mestre H, Nedergaard M (2018) The glymphatic pathway in neurological disorders. Lancet Neurol 17: 1016-1024.
4. Bohr T, Hjorth PG, Holst SC, Hrabetova S, Kiviniemi V, et al. (2022) The glymphatic system: Current understanding and modeling. iScience 25: 104987.
5. Christov IC (2021) Soft hydraulics: from Newtonian to complex fluid flows through compliant conduits. J Phys Condens Matter 34.
6. Ray L, Iliff JJ, Heys JJ (2019) Analysis of convective and diffusive transport in the brain interstitium. Fluids Barriers CNS 16: 6.
7. Schreder HE, Liu J, Kelley DH, Thomas JH, Boster KAS (2022) A hydraulic resistance model for interstitial fluid flow in the brain. J R Soc Interface 19: 20210812.
8. Thomas JH (2019) Fluid dynamics of cerebrospinal fluid flow in perivascular spaces. J R Soc Interface 16: 20190572.
9. Wardlaw JM, Benveniste H, Nedergaard M, Zlokovic BV, Mestre H, et al. (2020) Perivascular spaces in the brain: anatomy, physiology and pathology. Nat Rev Neurol 16: 137-153.
10. Babbs CF (2023) A new mechanism for glymphatic flow of interstitial fluid in branched perivascular spaces of the brain. Weldon School of Biomedical Engineering Faculty Working Papers: https://docs.lib.purdue.edu/bmewp/29.
11. Gouveia-Freitas K, Bastos-Leite AJ (2021) Perivascular spaces and brain waste clearance systems: relevance for neurodegenerative and cerebrovascular pathology. Neuroradiology 63: 1581-1597.

12. Evensen KB, Eide PK (2020) Measuring intracranial pressure by invasive, less invasive or non-invasive means: limitations and avenues for improvement. Fluids Barriers CNS 17: 34.
13. Babbs CF (2000) Efficacy of interposed abdominal compression-cardiopulmonary resuscitation (CPR), active compression and decompression-CPR and Lifestick CPR: basic physiology in a spreadsheet model. Crit Care Med 28: N199-202.
14. Chatelin S, Constantinesco A, Willinger R (2010) Fifty years of brain tissue mechanical testing: from in vitro to in vivo investigations. Biorheology 47: 255-276.
15. Tarasoff-Conway JM, Carare RO, Osorio RS, Glodzik L, Butler T, et al. (2015) Clearance systems in the brain-implications for Alzheimer disease. Nat Rev Neurol 11: 457-470.
16. Wang P, Olbricht WL (2011) Fluid mechanics in the perivascular space. J Theor Biol 274: 52-57.
17. Kedarasetti RT, Drew PJ, Costanzo F (2020) Arterial pulsations drive oscillatory flow of CSF but not directional pumping. Sci Rep 10: 10102.
18. Kazimierska A, Kasprowicz M, Czosnyka M, Placek MM, Baledent O, et al. (2021) Compliance of the cerebrospinal space: comparison of three methods. Acta Neurochir (Wien) 163: 1979-1989.